

Phase Jump Detector

Viotto, Sofia^{1*} and Bookhagen, Bodo¹

*Corresponding author

¹Institute of Geosciences, University of Potsdam

E-mails: viotto1@uni-potsdam.de

¹ 1 Introduction

2 The differential interferometric synthetic aperture radar (DInSAR) technique utilizes the phase
3 difference between two SAR scenes acquired at different times. The differential phase (known
4 as an interferogram) provides valuable information about the surface, enabling the detection
5 and measurement of ground motion. Accurately retrieving the magnitude of the movement
6 depends on several steps throughout the DInSAR processing chain. This description focuses
7 on scene alignment, the first and crucial step.

8 The purpose of scene alignment is to match common objects in an image pair while ensuring that
9 these objects are correctly positioned on the Earth's surface. Typically, alignment is performed
10 throughout coregistration and using precise knowledge of orbital parameters, together with
11 topographic information (Sansosti et al., 2006). However, the accuracy requirements for this
12 procedure vary depending on the SAR data acquisition mode, and finer alignment methods
13 may be needed. Thus, the accuracy demands for the Terrain Observation with Progressive
14 Scans (TOPS) mode are significantly higher, compared to the Stripmap mode (e.g., Prats-
15 Iraola et al., 2012; Yagüe-Martínez et al., 2016). The free data with global coverage provided
16 by the Sentinel-1 SAR mission, is mostly acquired in Interferometric Wide-Swath (TOPS) mode
17 (Torres et al., 2012).

18 In TOPS mode, the swath coverage is divided into subbands, which are captured in bursts
19 (De Zan and Monti Guarnieri, 2006). To generate a continuous DInSAR product, TOPS

20 bursts must be accurately matched and aligned in both the azimuth (along-track) and range
 21 (across-track) directions. Azimuth alignment must be better than 0.001 size of an azimuth
 22 cell size (Prats-Iraola et al., 2012; Wang et al., 2017; Fattahi et al., 2017). This accuracy
 23 requirement is significantly stricter than that for the range direction (i.e., 0.1 pixel of a range
 24 cell; Yagüe-Martínez et al., 2016).

25 Poor azimuth alignment introduces a ramp (i.e., a phase bias) within the TOPS burst inter-
 26 ferogram, as well as a linear ramp along the along-track direction over the entire interferogram
 27 (De Zan and Monti Guarnieri, 2006). Since these ramps are cyclic among consecutive bursts
 28 (i.e., they reset at each burst boundary), they are manifested as phase jumps along the over-
 29 lapping areas of consecutive bursts (cf. Figure1) (Fattahi et al., 2017).

A. Effects of Phase Jumps on Filtered and Unwrapped Interferograms

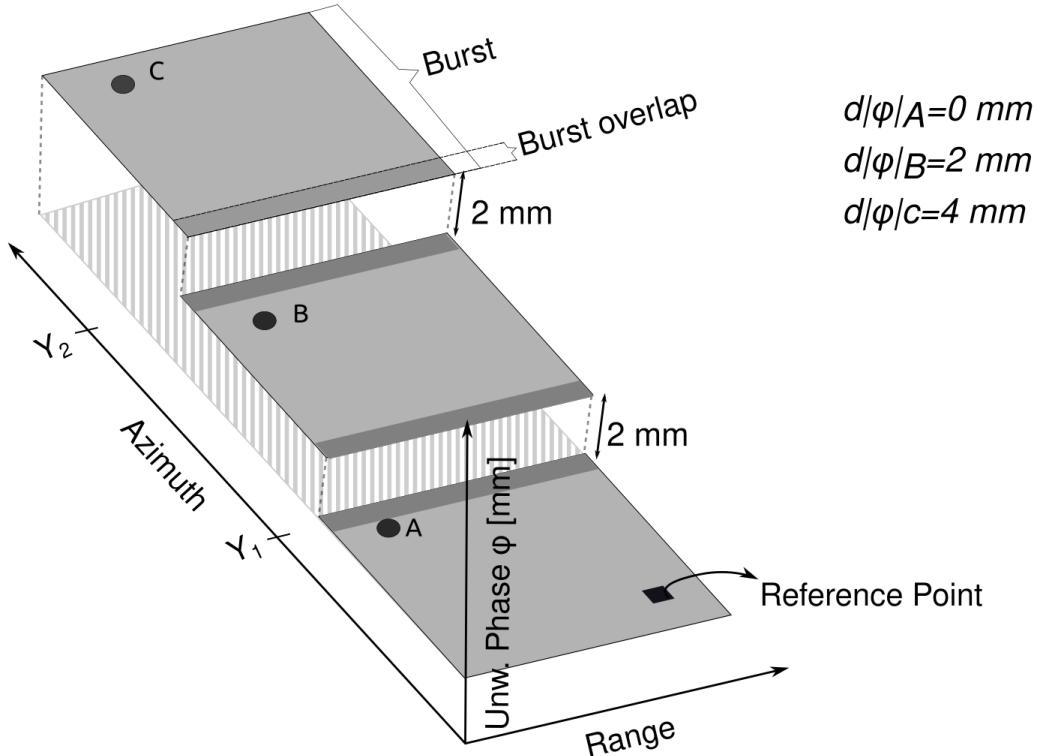


Figure 1: Conceptual drawing of the effects of phase jumps on filtered and unwrapped interferograms.

30 The azimuth misalignment is minimized through specific processing methods, such as Enhanced
 31 Spectral Diversity (ESD) (Prats-Iraola et al., 2012) and its variants (e.g., Fattahi et al., 2017;
 32 Wang et al., 2017). However, azimuth alignment may still be suboptimal, leading to small-

33 magnitude phase jumps that remain noticeable at burst boundaries. Subsequent steps, such as
34 multilooking and filtering of the wrapped phase, may obscure these jumps, but they will still
35 be visible in the unwrapped phase.

36 Identifying and quantifying phase jumps is a time-consuming process, particularly in datasets
37 containing thousands of interferograms. Furthermore, manual inspection does not allow mea-
38 surement of the magnitude of these jumps. To address this, we present an algorithmic approach
39 that helps users to 1) detect phase jumps at burst boundaries; 2) measure their magnitude; 3)
40 examine outliers; and 4) identify pairs or dates for exclusion from interferometric analysis. In
41 the following, we discuss its implementation.

42 2 Detection of Phase Jump at Burst Boundary

43 Building on the ideas of Zhong et al. (2014) and Wang et al. (2017), we developed an algo-
44 rithm to detect systematic phase jumps in unwrapped interferograms and quantify them using
45 statistical techniques. We focus on the residual effects of phase jumps at burst boundaries,
46 which are measured exclusively in the unwrapped phase. These phase jumps, when observed
47 in the wrapped phase and in the absence of filtering or multilooking, resemble a Heaviside step
48 function near the burst overlap. However, since filtering or multilooking is often applied before
49 phase unwrapping, these phase jumps in unwrapped interferograms are more likely to resemble
50 a sigmoid function.

51 The detection of phase jumps at burst boundaries is based on five key principles:

52 1. **Parsimony principle:** In a well-behaved unwrapped phase signal, the difference between
53 adjacent cells is expected to be small. In other words, the values of adjacent cells should
54 follow a smooth variation in the absence of significant deformation gradients. Phase jumps
55 fail to follow this principle, which constitutes the key point of the phase jump detection.

56 2. **Systematic phase jumps:** for a given pair, a phase jump in the burst overlap area is
57 systematic. This means that all cells along a specific azimuth coordinate (corresponding
58 to the burst overlap) exhibit a phase shift. One can think of this phase jump as an abrupt
59 disruption in phase continuity along azimuth.

60 3. **Consistency across interferograms:** phase jumps consistently appear at the same
61 coordinates across multiple interferograms. This is based on the fact that interferometry
62 with TOPS mode requires perfectly synchronized bursts (De Zan and Monti Guarnieri,
63 2006). Although this principle applies to Sentinel-1 (Torres et al., 2012) and TerraSAR-X
64 (Prats-Iraola et al., 2012) missions, it may not hold for non-synchronous TOPS acquisi-
65 tions such as the SAOCOM mission (e.g., Euillades et al., 2024).

66 4. **Significance of phase jumps:** If significant enough, phase jumps at burst boundaries
67 can produce residuals that remain detectable in the unwrapped phase. This is true even af-
68 ter the multilooking and filtering steps have been applied to the wrapped phase. However,
69 the detectability and prominence of phase jumps may vary depending on how consecu-
70 tive TOPS-interferogram bursts are stitched together (e.g., averaging across overlapping
71 areas, pasting the first burst onto the following one, etc.).

72 5. **Prevalence of phase jumps at burst boundaries in stacks of data:** Prevalence
73 implies that most of the data set have a certain percentage of pairs with notorious or
74 significant enough phase jumps at burst boundary coordinates.

75 To address the problem of detecting phase jumps at burst overlap, we divide it into two subprob-
76 lems. Firstly, we identify the coordinates where interferogram bursts were merged. Secondly,
77 we measure their magnitude, aiming to detect pairs with large phase jumps.

78 3 Identifying Burst Boundary Coordinates

79 3.1 Data Selection and Preparation

80 We perform a first-order selection of the pairs that can be evaluated. Pairs with extremely low
81 coherence (we define this as a median coherence below 0.4) cannot be effectively assessed, as
82 they lack sufficiently large areas to detect phase jumps.

83 The remaining pairs are masked based on their corresponding coherence. Cells with a coherence
84 value lower than a predefined value (typically 0.75) are masked throughout the evaluation. The
85 masking procedure aims to remove local phase jumps caused by processes other than azimuth

86 misalignment (e.g., speckle noise, deformation).
 87 Consider a data set of R pairs of interferograms with dimensions $(Y \times X)$ in radar coordinates,
 88 where Y is the total number of rows (azimuth direction) and X is the total number of columns
 89 (range direction). For a given pair r , the unwrapped phase (ϕ) at a cell location (i,j) is
 90 considered reliable if the coherence ($\gamma_{(r,i,j)}$) meets the following condition (Eq. (1)):

$$\phi_{(r,i,j)} = \begin{cases} \phi_{(r,i,j)}, & \text{if } \gamma_{(r,i,j)} > 0.75 \\ \text{No Data,} & \text{otherwise} \end{cases} \quad (1)$$

91 Note that i is a coordinate along the azimuth direction ($i \in Y$) and j along the range direction
 92 ($j \in X$).

93 3.2 Quantifying Phase Gradient

94 We calculate the absolute gradient of the unwrapped phase ($|\partial\phi/\partial Y|$) along the azimuth di-
 95 rection Y (hereafter referred to as phase gradient). The phase gradient is derived as follows:

$$\left| \frac{\partial\phi_{(r,i,j)}}{\partial Y} \right| = \begin{cases} |\phi_{(r,i,j)} - \phi_{(r,i+1,j)}|, & \text{if } i < Y \\ 0, & \text{if } i = Y \end{cases} \quad (2)$$

96 Note that when the row i equals the total number of rows Y , the phase gradient equals zero.
 97 In this way, the phase gradient maintains the same number of rows and columns $(Y \times X)$ as
 98 the unwrapped phase.

99 3.3 Classifying the Phase Gradient

100 To systematically distinguish cells with significant phase gradients, we classify the phase gra-
 101 dient. The classified gradient ($clas_{(r,i,j)}$), is defined by the following rules:

$$clas_{(r,i,j)} = \begin{cases} \text{No Data,} & \text{if } \left| \frac{\partial \phi_{(r,i,j)}}{\partial Y} \right| = \text{No Data} \\ 1, & \text{if } \left| \frac{\partial \phi_{(r,i,j)}}{\partial Y} \right| > M_{(r)} \\ 0, & \text{otherwise} \end{cases} \quad (3)$$

102 where $M_{(r)}$ is the median absolute phase gradient per pair: $M_{(r)} = median_r(\left| \frac{\partial \phi_{(r,i,j)}}{\partial Y} \right|)$. The
103 suffix r in the median indicates that the operation is performed along the dimension r .

104 The median $M_{(r)}$ is typically a small value, near half a millimeter, which confirms that the
105 parsimony principle holds on a large scale.

106 According to Eq. (3), the gradient is considered significant if its value is greater than the
107 median phase gradient of the pair.

108 3.4 Summarizing the Classified Gradient on a Row-Wise Basis

109 From the classified phase gradient, we derive a new property to identify phase jumps on a row-
110 wise basis. The phase-gradient intensity is the proportion of cells along a row with significant
111 phase gradient (i.e., cells marked with 1 in Eq. (3)). We only consider unmasked cells. We
112 refer to the phase-gradient intensity as intensity, and it is expressed as:

$$int_{(r,i)} = \frac{\sum_{j=1}^{j=X} clas_{(r,i)}}{C_{(r,i)}} \times 100 \quad (4)$$

113 With $int_{r,i}$ the intensity and $C_{r,i}$ the number of unmasked cells per row.

114 Note that, for a given pair r , the $int_{(r,i)}$ and $C_{(r,i)}$ variables have dimension (Y), which means
115 that the X dimension has been compressed.

116 Eq. (4) provides an indicator of the systematic nature of the phase jump. The closer the
117 value is to 100%, the greater the likelihood that the row corresponds to a phase jump at burst
118 overlap. Conversely, local phase jumps will have lower intensity values. Although the intensity
119 allows comparing different rows regardless of the number of unmasked cells, it also assigns the
120 same relevance to rows with an extremely low cells. This issue is addressed in the next section.

121 3.5 Detecting the Coordinates of Burst Overlap

122 We rely on the intensity to detect the overlap of the bursts and their coordinates. It should
 123 be noted that we detect these coordinates rather than deduce them from the regularity of the
 124 burst.

125 Before detecting the coordinates, it is necessary to preprocess the intensity data. Preprocessing
 126 includes applying row-reliability masking followed by data detrending.

127 The reliability of a row is determined by its number of unmasked cells ($C_{(r,i)}$). In most cases,
 128 this number is smaller than the total number of cells per row (i.e., $C_{(r,i)} < X$). However, the
 129 fewer cells a row contains, the less reliable it is. To set an appropriate threshold to define
 130 reliable rows, we apply a dynamic selection approach.

131 Dynamic selection compares the percentile of the distribution of unmasked cells (C), with the
 132 percentage p_k of the total cells per row X . Both percentile and percentage are calculated for a
 133 predefined value k (typically k equals 25). At the end, the threshold t is set to be equal to the
 134 largest value ($t = P_k$ if $P_k > p_k$, otherwise $t = p_k$).

135 Once the threshold of row reliability is established, we mask the intensity as follows:

$$int_{(r,i)} = \begin{cases} \text{No Data,} & \text{if } C_{(r,i)} < t \\ int_{(r,i)}, & \text{otherwise} \end{cases} \quad (5)$$

136 In a posterior stage, the masked intensity is detrended. The trend arises from gradients in
 137 coherence along the azimuthal direction, resulting in gradients in intensity. The existence of
 138 these gradients makes it difficult to compare rows in order to detect burst overlaps. We remove
 139 this trend by dividing each row by its median intensity across pairs as:

$$int_{(r,i)}^d = \frac{int_{(r,i)}}{median_{r,i}(int_{(r,i)})} \quad (6)$$

140 with $int_{(r,i)}^d$ the detrended intensity and $median_{r,i}$ the median of the i -row across all pairs.

141 We obtain the gradient along the Y dimension from the detrended intensity. This gradient
 142 allows us to obtain the coordinates of peaks in the intensity. The gradient is computed as Eq.

143 (7).

$$\frac{\partial \text{int}_{(r,i)}^d}{\partial Y} = \begin{cases} \text{int}_{(r,i)}^d - \text{int}_{(r,i+1)}^d, & \text{if } i < Y \\ 0, & \text{if } i = Y \end{cases} \quad (7)$$

144 where $\text{int}^d(r, i)$ is the detrended intensity, and $\partial \text{int}_{(r,i)}^d / \partial Y$ represents its gradient along the Y
 145 dimension. To avoid confusion with the gradient defined in Eq. (2), we will refer to it as the
 146 gradient of intensity.

147 Next, we detect the i -coordinates where the gradient of intensity peaks. A peak is detected if
 148 the gradient of intensity is three times larger than the standard deviation:

$$\text{coord}_{ovlp} = \begin{cases} i, & \text{if } \frac{\partial \text{int}_{(r,i)}^d}{\partial Y} > \left(3 \times \text{std}(\frac{\partial \text{int}^d}{\partial Y}) \right) \\ \text{No Data}, & \text{otherwise} \end{cases} \quad (8)$$

149 With coord_{ovlp} the coordinates of burst overlaps, and std the standard deviation which is derived
 150 from the whole dataset. This stage is known a *coarse coordinates detection*.

151 We analyze the set of coord_{ovlp} detected in the previous step. We denominate this stage as
 152 *coordinates refinement*. Ideally, the same coordinates should appear in all pairs if they align
 153 with the burst overlaps. However, this may not be the case if the masks fail to identify and
 154 remove unreliable rows.

155 To refine the coordinates, we separate them into b groups. The number of groups corresponds to
 156 the expected number of burst overlaps (i.e., $b = B - 1$). Each group is centered on a theoretical
 157 i -coordinate matching a burst overlap position. For each burst overlap number, the central
 158 coordinate is given by the size of the burst ($\sim (Y/B)$) multiplied by the burst overlap number.
 159 Thus, the central coordinate at a given burst overlap number n is:

$$i_n^c = \text{int}(Y/B) * n \quad (9)$$

160 Where i_n^c is the central coordinate, and int denotes integer division. The burst number n ranges
 161 from 1 to b .

- 162 We establish the limits of each group as half of the burst coordinates after and before its central
163 coordinate (i.e., $i_n^c \pm (\text{int}(Y/B) * 0.5)$).
164 Within each group, we store the most frequent coordinate found. Ideally, this refinement
165 ends with b coordinates. In practice, if the pairs have generally low coherence, the number of
166 coordinates found may be less than b .

167 **3.6 Estimating Ramp by Phase Jump**

168 We measure the phase gradient (Eq. (2)) on a row-wise basis as the median phase gradient
169 per row ($pj_{r,i}$). We examine these medians only at the i -coordinates identified as burst overlap
170 during the refinement stage.

171 To estimate the overall ramp introduced by the phase jumps at the burst overlap, pj_r , we
172 compute the average of the phase jumps measured and multiply it by the number of burst
173 overlaps. Thus:

$$pj_r \sim \frac{\sum pj_{r,i}}{n_f} \times b \quad (10)$$

174 With n_f is the number of measured phase jumps at burst overlap, and this number can be
175 less than the number of burst overlaps (i.e., $n_f < b$). Note that if both values are equal (i.e.,
176 $n_f = b$), the ramp of the phase jumps is the sum of the gradients per row at a given pair.

177 **4 Detecting and Excluding Pairs**

178 Finally, we detect dates or pairs that should be excluded from further processing. In this case,
179 we establish a threshold for the maximum ramp (Eq. (10)) that a user can reasonably accept
180 (typically around half a centimeter). In this way, we identify pairs that exhibit a phase-jump-
181 derived ramp exceeding the predefined threshold. All these pairs should be excluded from time
182 series processing.

¹⁸³ 5 Code Implementation

¹⁸⁴ The algorithm is implemented in Python. It relies on the Miami InSAR Time-series software
¹⁸⁵ in Python (MintPy) (Yunjun et al., 2019). In addition, we use the *xarray* open-source package
¹⁸⁶ (Hoyer and Hamman, 2017) for labeling, organizing the data, and generating outputs. Other
¹⁸⁷ essential tools include *NumPy* (Harris et al., 2020) and *Matplotlib* (Hunter, 2007).

¹⁸⁸ We called the Python script *calculate_phasejumps_from_mintpystack.py* and it is available on
¹⁸⁹ github https://github.com/UP-RS-ESP/PhaseJumps_InSAR.

¹⁹⁰ 5.1 Input

¹⁹¹ The program requires as input a stack of pairs in *HDF5* format, generated using MintPy. The
¹⁹² stack contains a wrapped phase, an unwrapped phase, coherence, and a connected component
¹⁹³ mask for each pair.

¹⁹⁴ The stacks must be provided in radar coordinates and should cover the full dimension along the
¹⁹⁵ azimuth direction, meaning no subset should be applied along azimuth when loading the data
¹⁹⁶ with MintPy. Otherwise, the phase-jump coordinate refinement stage will fail. Additionally, if
¹⁹⁷ the stack results from the processing of two or three sub-swaths, an area of interest should be
¹⁹⁸ specified. The current implementation is not optimized for analyzing interferograms derived
¹⁹⁹ from the processing of multiple sub-swaths.

²⁰⁰ Input parameters to run the program are summarized in Table 1.

Table 1: Description of input parameters to run the program. Parameters indicated by **m** are mandatory, whereas parameters indicated with **o** are optional

Parameter	Description
<code>- -inDir</code>	[m] Working directory containing <i>input/ifgramStack.h5</i> . Format: <i>string</i>
<code>- -n-burst</code>	[m] Number of bursts processed to generate the interferograms. Format: <i>integer</i>

Parameter	Description (mandatory, optional)
<code>- -pct</code>	[o] Value k to define the row reliability masking threshold. Value in range 0.0-1.0. Format: <i>float</i> . Default: 0.25 (Eq. (5))
<code>- -cmin</code>	[o] Minimum coherence of pixels to be assessed (in range 0 to 1). Format: <i>float</i> . Default: 0.75 (Eq. (1))
<code>- -msk-avgCoh</code>	[o] Use an additional mask based on the average coherence of the stack. The option is automatically activated in case of poor coherence. Default: <i>Deactivated</i>
<code>- -pj-thr</code>	[o] Maximum accumulated phase jump per pair in milliliter. Format: <i>float</i> . Default: 5
<code>- -sub-x</code>	[o] Area of interest along the range direction ($x_0 x_1$). Specify it in case of stacks generated after merging two or three subswaths. Format: <i>integer integer</i> .
<code>- -pair</code>	[o] Perform calculations only for a pair. Format: <i>YYYYMMDD_yyyymmdd</i>
<code>- -plot-ind</code>	[o] Plot every interferogram from the stack, altogether with the intensity mask. Default: <i>Deactivated</i>

201 5.2 Output

202 Output are saved in the working directory, within the subdirectory called *pj_evaluation*. Figures
203 are stored in the subdirectory *pj_evaluation/figs*.

204 Output arrays are saved in netCDF format. The files have dimensions (*pair* \times *Y*), with *pair*
205 the pair name (*pair* = *R*) and *Y* the azimuth coordinate. Dimension *pair* contains the pair
206 names stored in string format as *YYYYMMDD_yyyymmdd* (year, month, day). Dimension *Y*
207 contains azimuth row label (in radar coordinates), with integer format.

208 Output naming convention of arrays follows the rule "variable_unit" (Table 2). File name
209 suffixes have the following meanings:

Coherence-based Row Reliability

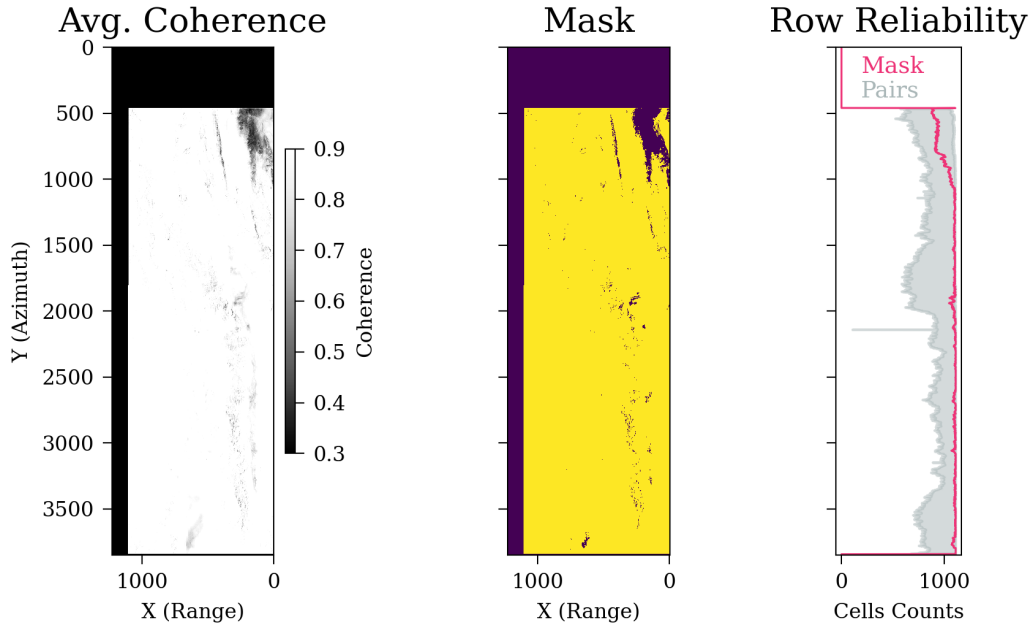


Figure 2: Example Output for the generation of the coherence mask.

210 • $_pct$: percentage

211 • $_cts$: counts

212 • $_mm$: millimeter

213 In case a pair is selected (with *pair* parameter), then all output arrays end with the pair name

214 in format YYYYMMDD_ $yyyymmdd$.

Table 2: Description of nc output files generated by the algorithm. Output files indicated with * are only generated in case of activating the corresponding function.

File Name	Description
<i>intensity_pct.nc</i>	Intensity per row (Eq. (4)). Dimensions: (<i>pair</i> \times <i>Y</i>). Format: <i>Int16</i> , No Data: -999
<i>coherence_cts.nc</i>	Number of unmasked cells per row (i.e., number of pixels with coherence $> cmin$), after coherence masking on cell-wise basis (Eq. (1)). Dimensions: (<i>pair</i> \times <i>Y</i>). Format file: <i>Int16</i> , No Data: -999

File Name	Description
<i>median_az_grad_mm.nc</i>	Median absolute gradient per row (i.e. along azimuth direction) in millimeter unit. Dimensions: $(pair \times Y)$. Format: <i>float32</i>
<i>maskCoh_cts.nc</i>	[*] Number of unmasked cells per row (coherence $> cmin$), from the average coherence of the data set. Saved if the option <i>msk-avgCoh</i> is activated. Dimensions: $(pair \times Y)$. Format file: <i>Int16</i> , No Data: -999

215 Additional output files are provided in text format (*.txt*). They contain all relevant information
 216 for the evaluation, such as statistics as well as the results of the phase jump evaluation (Table
 217 3).

Table 3: Description of output text files generated by the algorithm

File Name	Description
<i>stats_absolute_gradient.txt</i>	File containing summarized statistics (average, median, standard deviation) of coherence and absolute phase gradient (Eq. (2)), as well as the temporal baseline per pair from the stack.
<i>magnitude_phase_jumps.txt</i>	File containing the overall magnitude of the phase jump, which is estimated with Eq. (10). Note that this magnitude is estimated only from pairs that are not excluded from the assessment (i.e., pairs with a median coherence > 0.4).
<i>exclude_listdate12_interferogram_s_by_phase_jump.txt</i>	File containing all pairs that should be excluded from the assessment. This file includes pairs that were excluded from the assessment (median coherence below 0.4). Pairs are presented in two ways: by pair name (format YYYYMMDD_yyyyymmdd) and by the index that the pair has in the stack.

File Name	Description
<i>exclude_dates_by_phase_jumps</i> .txt	File containing dates that should be excluded from the assessment if more than 50% of their pairs exhibit a significant phase jump

Preprocessing of intensity

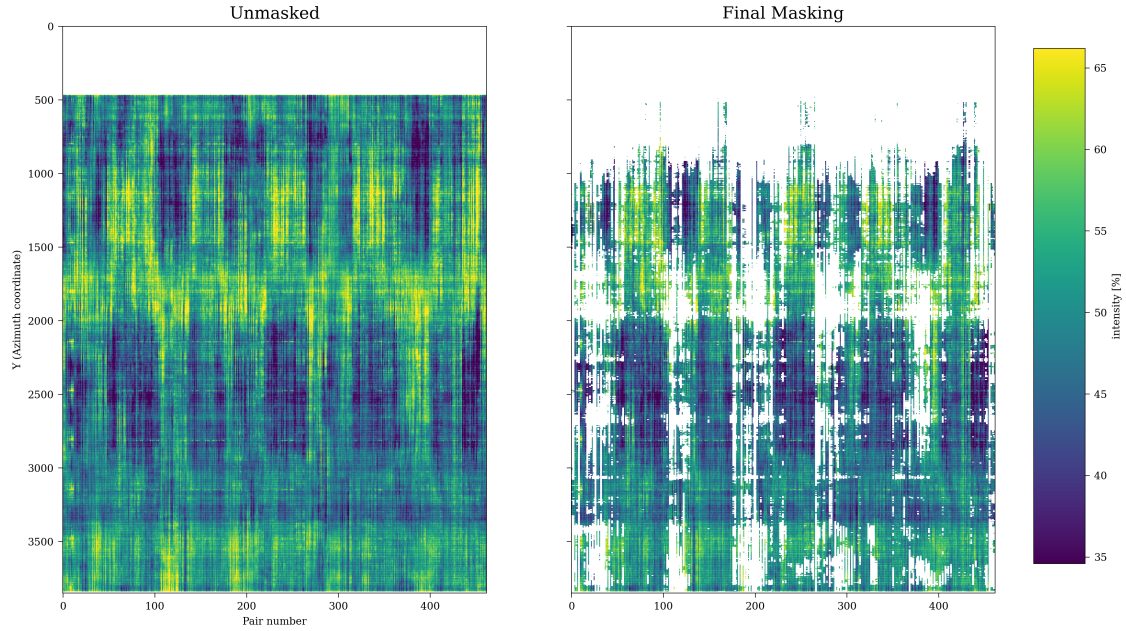
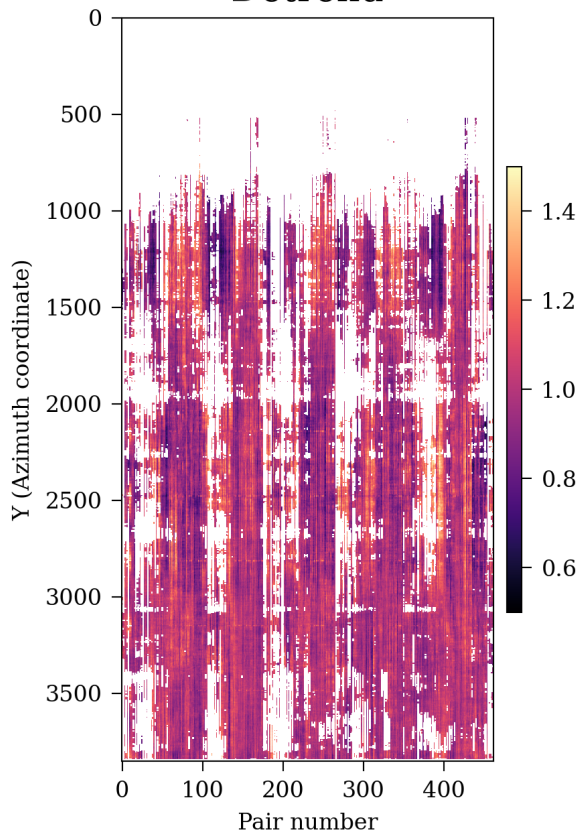


Figure 3: Example Output of the masked intensity

Detection of Phase Jump at Burst Overlap

Detrend



Gradient

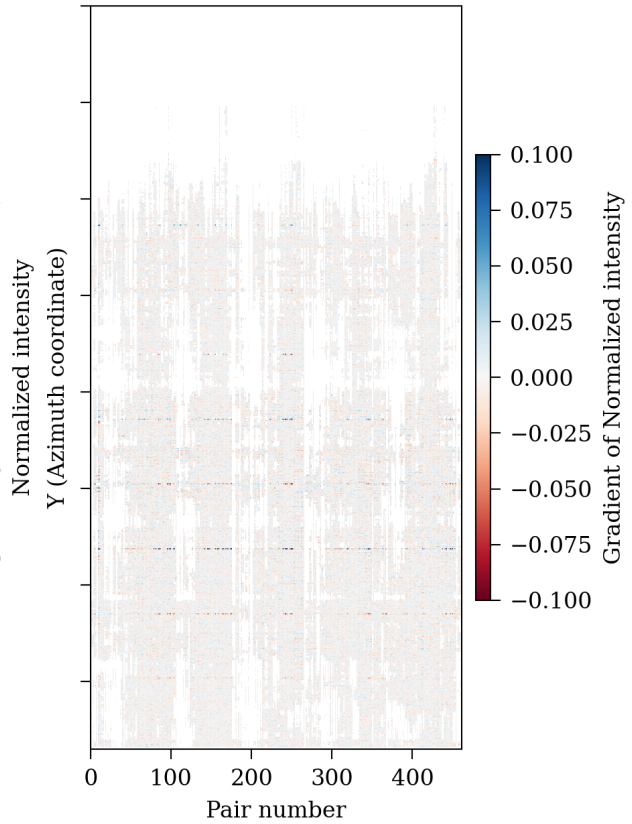


Figure 4: Example Output for the detrended intensity.

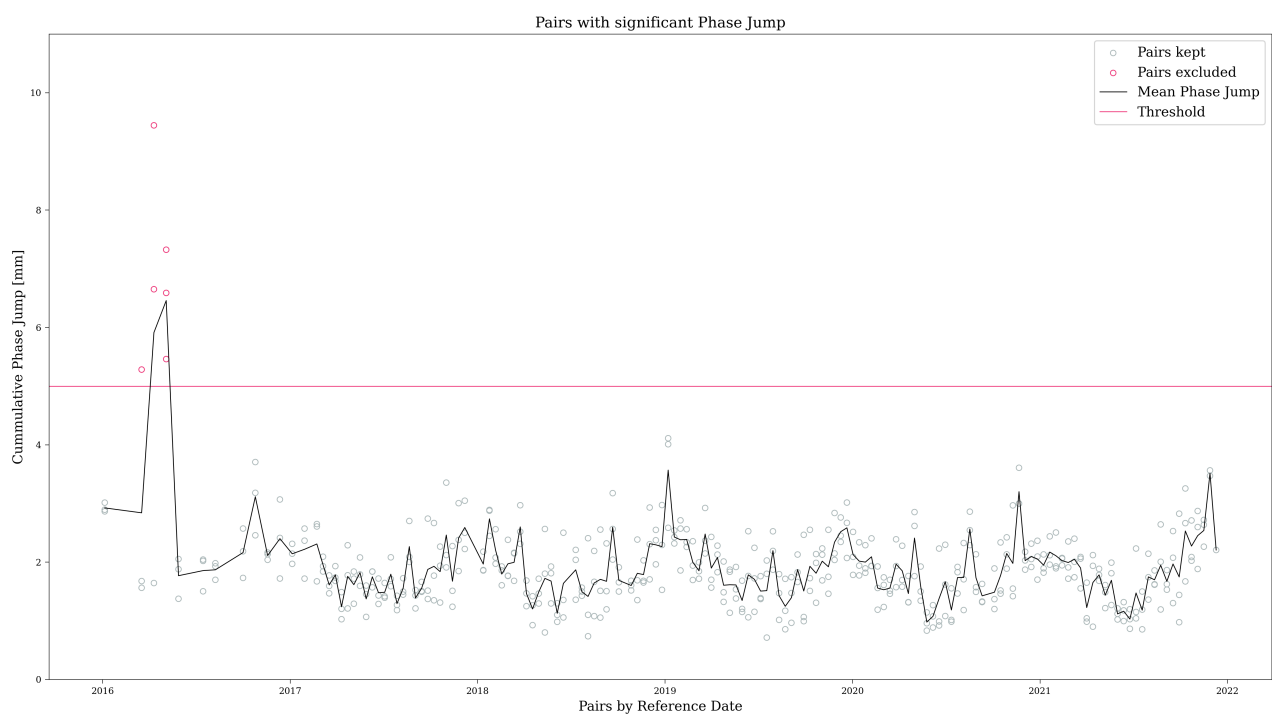


Figure 5: Example Output for a time series showing estimated phase jump magnitude for every date.

218 **References**

- 219 De Zan, F. and Monti Guarneri, A. (2006). Topsar: Terrain observation by progressive scans.
220 *IEEE Transactions on Geoscience and Remote Sensing*, 44(9):2352–2360.
- 221 Euillades, J. A., Roa, Y. L., Euillades, L. D., Euillades, P. A., Rosell, P. A., Solarte, E. A., and
222 Perna, S. (2024). Interferometric assessment of saocom-1 topsar data. *IEEE Geoscience and*
223 *Remote Sensing Letters*, 21:1–5.
- 224 Fattah, H., Agram, P., and Simons, M. (2017). A network-based enhanced spectral diver-
225 sity approach for tops time-series analysis. *IEEE Transactions on Geoscience and Remote*
226 *Sensing*, 55(2):777–786.
- 227 Harris, C. R., Millman, K. J., van der Walt, S. J., Gommers, R., Virtanen, P., Cournapeau,
228 D., Wieser, E., Taylor, J., Berg, S., Smith, N. J., Kern, R., Picus, M., Hoyer, S., van
229 Kerkwijk, M. H., Brett, M., Haldane, A., Fernández del Río, J., Wiebe, M., Peterson, P.,
230 Gérard-Marchant, P., Sheppard, K., Reddy, T., Weckesser, W., Abbasi, H., Gohlke, C., and
231 Oliphant, T. E. (2020). Array programming with NumPy. *Nature*, 585:357–362.
- 232 Hoyer, S. and Hamman, J. (2017). xarray: N-d labeled arrays and datasets in python. *Journal*
233 *of Open Research Software*.
- 234 Hunter, J. D. (2007). Matplotlib: A 2d graphics environment. *Computing in Science & Engi-*
235 *neering*, 9(3):90–95.
- 236 Prats-Iraola, P., Scheiber, R., Marotti, L., Wollstadt, S., and Reigber, A. (2012). Tops interfer-
237 ometry with terrasar-x. *IEEE Transactions on Geoscience and Remote Sensing*, 50(8):3179–
238 3188.
- 239 Sansosti, E., Berardino, P., Manunta, M., Serafino, F., and Fornaro, G. (2006). Geometrical
240 sar image registration. *IEEE Transactions on Geoscience and Remote Sensing*, 44(10):2861–
241 2870.
- 242 Torres, R., Snoeij, P., Geudtner, D., Bibby, D., Davidson, M., Attema, E., Potin, P., Rommen,
243 B., Flourey, N., Brown, M., Traver, I. N., Deghaye, P., Duesmann, B., Rosich, B., Miranda,
244 N., Bruno, C., L'Abbate, M., Croci, R., Pietropaolo, A., Huchler, M., and Rostan, F. (2012).

- 245 Gmes sentinel-1 mission. *Remote Sensing of Environment*, 120:9–24. The Sentinel Missions
246 - New Opportunities for Science.
- 247 Wang, K., Xu, X., and Fialko, Y. (2017). Improving burst alignment in tops interferometry
248 with bivariate enhanced spectral diversity. *IEEE Geoscience and Remote Sensing Letters*,
249 14(12):2423–2427.
- 250 Yagüe-Martínez, N., Prats-Iraola, P., Rodríguez González, F., Brčic, R., Shau, R., Geudtner,
251 D., Eineder, M., and Bamler, R. (2016). Interferometric processing of sentinel-1 tops data.
252 *IEEE Transactions on Geoscience and Remote Sensing*, 54(4):2220–2234.
- 253 Yunjun, Z., Fattah, H., and Amelung, F. (2019). Small baseline insar time series analysis:
254 Unwrapping error correction and noise reduction. *Computers & Geosciences*, 133:104331.
- 255 Zhong, H., Tang, J., Zhang, S., and Zhang, X. (2014). A quality-guided and local minimum
256 discontinuity based phase unwrapping algorithm for insar/insas interferograms. *IEEE Geo-
257 science and Remote Sensing Letters*, 11(1):215–219.